Nuclear Engineering and Design 305 (2016) 389–399

Contents lists available at ScienceDirect

Nuclear Engineering and Design

journal homepage: www.elsevier.com/locate/nucengdes

Oxidation effects during corium melt in-vessel retention

V.I. Almyashev [a], V.S. Granovsky [a], V.B. Khabensky [a], E.V. Krushinov [a], A.A. Sulatsky [a], S.A. Vitol [a], V.V. Gusarov [b], S. Bechta [c], M. Barrachin [d], F. Fichot [d], P.D. Bottomley [e,*], M. Fischer [f], P. Piluso [g]

[a] Alexandrov Scientific-Research Institute of Technology (NITI), Sosnovy Bor, Russia
[b] Ioffe Institute, St. Petersburg, Russia
[c] Royal Institute of Technology (KHT), Stockholm, Sweden
[d] Institut de Radioprotection et de Sûreté Nucléaire (IRSN), St Paul lez Durance, France
[e] Joint Research Centre, Institut für Transurane (ITU), Karlsruhe, Germany
[f] AREVA GmbH, Erlangen, Germany
[g] CEA Cadarache-DEN/DTN/STRI, France

HIGHLIGHTS

- Corium–steel interaction tests were re-examined particularly for transient processes.
- Oxidation of corium melt was sensitive to oxidant supply and surface characteristics.
- Consequences for vessel steel corrosion rates in severe accidents were discussed.

ARTICLE INFO

Article history:
Received 22 January 2016
Received in revised form 20 May 2016
Accepted 24 May 2016
Available online 23 June 2016

JEL classification:
C. Material Properties

ABSTRACT

In the in-vessel corium retention studies conducted on the Rasplav-3 test facility within the ISTC METCOR-P project and OECD MASCA program, experiments were made to investigate transient processes taking place during the oxidation of prototypic molten corium. Qualitative and quantitative data have been produced on the sensitivity of melt oxidation rate to the type of oxidant, melt composition, molten pool surface characteristics. The oxidation rate is a governing factor for additional heat generation and hydrogen release; also for the time of secondary inversion of oxidic and metallic layers of corium molten pool.

1. Introduction

Melt oxidation is one of the principal processes influencing the condition of molten corium pool formed in the reactor vessel bottom in the course of PWR, BWR and VVER severe accident progression. Limited mass of water during core re-flood and residual water in the vessel lower head cannot produce enough steam for complete oxidation of fuel, clad and core structural materials (Zr), so the in-vessel corium is considerably suboxidized, i.e. the molten pool contains active reducing agents (U, Zr). Elements of relocated stainless steel of in-vessel structures (Fe, Cr, Ni, Mn, ...), control rods (Ag, Cd, In, B, C) and reactor pressure vessel (Fe, C, ...) also belong to this category of redox reaction elements.

On the other hand, during or after the molten pool formation the oxidant can also get access to the pool surface: either water supplied into the vessel or due to the mass exchange between the in-vessel gas atmosphere and steam of the containment. In this case the redox reactions can bring changes to the molten pool structure and composition, as can hydrogen generation and additional heat deposition in the melt. It is therefore necessary to simulate the above-mentioned phenomena in the analysis of melt in-vessel retention (IVR), uncooled vessel failure and hydrogen safety.

In (Khabensky et al., 2003, 2011; Asmolov et al., 2007, 2006; Bechta et al., 2010) the oxidation phenomena of prototypic corium having different compositions and oxidizing atmosphere have been studied in the small-scale experimental facilities. In Sulatsky et al. (2013) results of these studies are analyzed. It was established that practically in all cases the oxidation is in the starvation mode, i.e. its rate is limited by the flow rate of oxidant supply to the melt surface. It is noted that surface oxidic crust provides an additional diffusion barrier and reduces the oxidation rate. References Asmolov et al. (2007) and Sulatsky et al. (2013) also give some

* Corresponding author. Tel.: +49 7247 951 364; fax: +49 7247 951 593.
E-mail address: paul.bottomley@ec.europa.eu (P.D. Bottomley).

http://dx.doi.org/10.1016/j.nucengdes.2016.05.024
0029-5493/

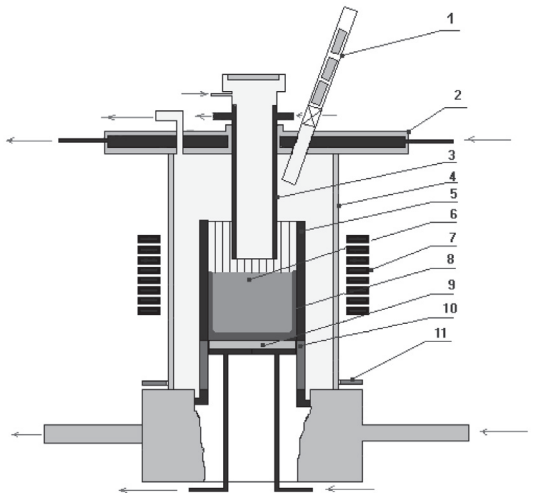

Fig. 1. Rasplav-3 induction furnace schematics. (1) Port for metal introduction; (2) furnace cover; (3) pyrometer shaft flushed with argon; (4) quartz tube; (5) cold crucible sections; (6) corium melt; (7) inductor; (8) crust; (9) bottom calorimeter; (10) water-cooled electromagnetic screen; (11) shield of collector unit.

examples of secondary inversion of oxidic and metallic layers after sufficient oxidation of corium molten pool when an initial bottom U and Zr-rich metallic melt has occurred.

This paper gives further analysis of previous experimental data (Sulatsky et al., 2013) and new data about the effect of oxidic crusts.

2. Experimental

Experimental studies of the prototypic corium oxidation phenomena, which are discussed in this paper, were conducted on the Rasplav-3 tests facility of the RASPLAV platform in NITI within the ISTC METCOR-P project and OECD MASCA program. All experiments except MCP-6 used the technology of induction melting in a cold crucible. The induction furnace schematics is given in Fig. 1. In MCP-3 the bottom calorimeter (Fig. 1, item 9) was replaced by the water-cooled reactor vessel steel specimen. In experiments with steam used as the oxidant (MCP-3, MCP-6, MCP-7, MA-9) a practically identical gas-aerosol system was used, which is shown in Fig. 2. The gas-aerosol system schematics in the experiment with air (MA-7) is shown in Fig. 3.

In experiments with oxidic or oxidic-metallic melt (MCP-3, MCP-7, MA-7, MA-9) the initial corium oxidation index is approximately C-30 (that is 30% of the initial inventory of Zr (in moles) is oxidized to ZrO_2), and uranium–zirconium ratio $(U/Zr)_{at} \approx 1.2$. Table 1 in the Discussion (Section 3) summarises the conditions of the experiments together with major results.

2.1. Experiment MCP-3

Experiment MCP-3 was conducted within the METCOR-P project. The molten pool bottom lay on the flat surface of a cylindrical steel specimen inside the water-cooled crucible of induction furnace. The arrangement was the same as in experiments on the interaction between the suboxidized corium melt and reactor vessel steel (Bechta et al., 2004, 2006). The molten pool was produced in an argon atmosphere on the surface of specimen, the bottom of which was cooled with water. As a result of steel–melt interaction, the liquid–solid interaction zone (IZ) was formed at the specimen surface, which was separated from the melt by oxidic crust; its main components were Fe, U and Zr. At this stage (stage A) the experiment practically repeated experiment MC6 of METCOR (Bechta et al., 2004).

After that, by shifting the electromagnetic screen and crucible and reducing power deposition into the melt the massive oxidic crust was formed on the steel specimen surface; it was made in parallel with a substantial steel specimen temperature reduction (stage B). After that the above-melt argon atmosphere was replaced with steam. This atmosphere was maintained by steam supply with the flow-rate of approx. 400 g/h (111 mg/s). During 30 min (stage C) the melt was oxidized in the crust-free regime, excluding the startup and finish periods. During this, no water condensate was observed in the condenser installed in the gas line (see item 6 in Fig. 2). The massive oxidic crust on the steel surface prevented the IZ oxidation during stage C. Later, approximately within 1 h 20 min (stage D), crust thickness on the steel specimen surface was reduced to the value, from which the IZ oxidation process was started and completed (stage E). At this stage a part of the supplied steam did not interact with melt; it was evacuated from the furnace into the condenser (see items 5 and 6 in Fig. 2).

Fig. 4 illustrates oxidation processes at stages C and E by the corresponding correlations of hydrogen release versus time determined from the steam oxidation of the reducing agent components. Correlations (1) illustrate oxidation process at stages C and E.

$$U/Zr + 2H_2O = UO_2/ZrO_2 + 2H_2 \quad (1)$$

For stage C the hydrogen release rate was 9.9 mg H_2/s, and for stage E – 5 mg H_2/s. Taking into account the melt surface area (crucible inner diameter was 70 mm) the oxygen release rate per unit surface area is 0.26 for stage C and 0.13 mg $H_2/(cm^2\ s)$ for stage E. The corresponding values of the steam-melt mass interaction rate are 2.34 and 1.17 mg $H_2O/(cm^2\ s)$.

In MCP-3 it was difficult to determine concentration of H_2 which flowed out from the furnace in the carrier gas (N_2). The same problem was with the water condensate rate measurement. Therefore, the calculations of mentioned rates were made by measuring oxygen consumption for the oxidation of reducing agents in the corium melt and IZ. The methodology is explained in detail in Khabensky et al. (2011). This work also provides an insight into the melt surface condition. It follows that at brief time intervals in the beginning and in the end of stage C, also in the end of stage E, the melt surface was covered with crust. Therefore, for most of the time during both stages, the oxidic crust was not present on the melt surface.

2.2. Experiment MA-9

Experiment MA-9 (Asmolov et al., 2007) was conducted within the MASCA program. Initially the molten pool was established in the argon atmosphere (crucible inner diameter the same as in MCP-3 – 70 mm). Stainless steel was added (Kh18N10T), its mass fraction in the melt was 0.1. After reaching the state of equilibrium resulting from the component partitioning between the suboxidized corium and SS melts, the two-liquid molten pool was formed with the oxidic liquid in a surface position. After that steam was supplied to the above-melt atmosphere at a flow-rate of approx. 800 g/h (222 mg/s); the melt oxidation was going on for approx. 20 min. The analysis of post-experimental ingot revealed metallic layer was in the surface position, which indicated the inversion of oxidic and metallic liquids in the course of melt oxidation.

In MA-9 the flow rate of steam spent on the melt oxidation was calculated from the difference between the supplied steam and measured condensate mass at the furnace exit taking into account water collected by the filters. Fig. 5 shows the experimental data, according to which the melt oxidation rate was approximately steady, the interaction rate of the steam with the melt was 0.11 g H_2O/s, and the rate per unit surface area was 2.92 mg $H_2O/(cm^2\ s)$. In Sulatsky et al., 2013 the posttest analysis has shown

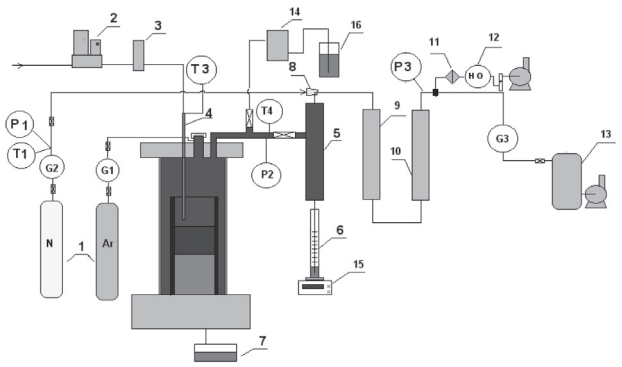

Fig. 2. Schematics of gas-aerosol system in experiments with steam. (1) Ar, N tanks; (2) water flow controller; (3) steam generator; (4) steam line in; (5) steam condenser; (6, 7) condensate bottles; (8) ejector; (9) large area filter (LAF); (10) silicagel dryer; (11) Petrianov filters (AFA); (12) oxygen and hydrogen electrochemical sensors; (13) vacuum receiver; (14) large area filter (LAF), startup line; (15) balance; (16) hydrolock.

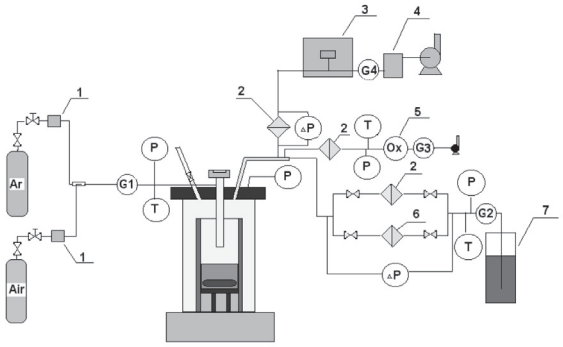

Fig. 3. Schematics of gas-aerosol system in experiment with air. (1) Dryer; (2) Petrianov filters (AFA); (3) mass-spectrometer; (4) vacuum tank; (5) oxygen sensor; (6) medium area filter (MAF); (7) hydrolock; (G1, G2) gas flow rate meters; (G3,G4) rotameters; P, pressure gauges, T, L-type thermocouples.

that the oxidation rate stays steady, irrespective of the amount and composition of reducing agents.

2.3. Experiment MCP-7

Experiment MCP-7 is not fully analyzed in Sulatsky et al. (2013) and Khabensky et al. (2011), therefore we are going to discuss it in more detail. The experiment was conducted within the METCOR-P project. In contrast to MA-9 the MCP-7 crucible inner diameter was 38 mm and a "UO_2–ZrO_2–Zr" pool of prototypic corium (no stainless steel) was produced, the crust was established on the melt surface before the steam supply to the furnace was started at a steady rate of 59 g H_2O/h. For the crust production, the melt surface was raised above the inductor coils, and so the melt surface temperature was lowered to below the system liquidus temperature.

Fig. 6 shows the experimental dynamics of condensate mass at the furnace exit, volumetric hydrogen content in the carrier gas (N_2) and the carrier gas flow rate. Strain gauge readings of the condensate weight (Fig. 2, item 15), excluding the brief starting and final periods, show the linear growth of the condensed steam mass.

Noteworthy are unstable readings of the hydrogen sensor. All efforts to stabilize them by changing the carrier gas flow rate at the 4990–5910 s and 7900–8400 s time intervals brought no results. Oscillations of the hydrogen sensor readings were also observed during the steady carrier gas supply period (e.g. 6000–7000 s). At 8037 s the indications grew sharply. At this moment, the crust swelling and partial spilling was observed in parallel with the sharp temperature growth of the molten pool surface. At 9042 s the steam supply was stopped and the furnace was flushed with Ar. At 9479 s heating was disconnected and the melt was frozen.

It should be noted that during the oscillations of hydrogen readings, cracks periodically appeared on the surface. Through them the melt was ejected and spread on the crust surface. The melt on the crust surface quickly became oxidized and crystallized.

Taking into account the instability of the measured hydrogen content in the carrier gas and, on the contrary, stable, close-to-linear growth of condensate mass at the furnace exit, the steam-melt interaction rate, as in MA-9, was calculated from the difference between the flow rate of supplied steam and the accumulation of condensate mass in the collector. Fig. 7 gives the results of measurements and calculations of this flow rate, which was approximately 8.1 mg H_2O/s, corresponding to a mass rate per unit surface area of 0.72 mg H_2O/(cm^2 s).

Fig. 8 shows the corium ingot surface after the furnace was opened. The ingot mass was approximately 1 kg, and the corium oxidation degree determined by the XRF and chemical analysis was C-61.

The following was found during the ingot inspection:

- Part of the crust is missing, it fell into the melt before the heating disconnection;
- Surface of the crust remaining on the periphery is uneven and has bulges; its thickness is 2–4 mm;
- Possibly deformation on cooling/solidification – judging by the difference in height between the ingot and remaining part of the crust (see Fig. 8); this is probably a gas cavity that existed between the melt and crust.

Table 1
Matrix of MCP-3,6,7 and MA-7 and 9 experiments.

Experiment	Initial molten pool	Surface crust	Melt/crust surface temperature, °C	Oxidant	Oxidant flow rate, mg/s	Mass rate of oxidant absorbed by the melt, mg/(cm^2 s)
MCP-3(1)	UO_2–ZrO_2–Zr pool (stage C)	Absent	2400	Steam	111	H_2O – 2.34
MCP-3(2)	Oxidic pool C-100, IZ oxidation (stage E)	Present above IZ in stage E	2400		111	H_2O – 1.17
MA-9	UO_2–ZrO_2–Zr pool, steel mass fraction ~0.1	Absent	2500		230	H_2O – 2.92
MCP-7	UO_2–ZrO_2–Zr pool	Present	2000		16.4	H_2O – 0.72
MCP-6	Molten steel with U and Zr	Present	1230		28.6 and 54.7	H_2O – 0.24
MA-7(1)	UO_2–ZrO_2–Zr pool, steel mass fraction ~0.1	Absent	2500	Air	197	O_2 – 1.17 N_2 – 3.74 Σ – 4.91
MA-7(2)		Present	2250		197	O_2 – 0.52 N_2 – 0.52 Σ – 1.04

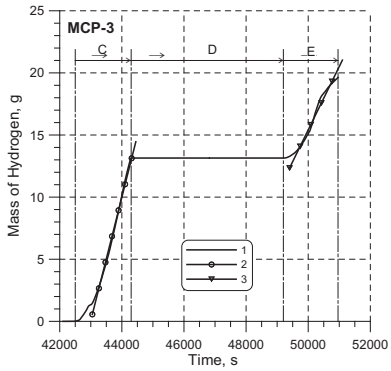

Fig. 4. Hydrogen release during oxidation of corium melt and IZ by steam in MCP-3 test. (1) Mass of released hydrogen; (2) interpolation for the steady regime of stage C; (3) interpolation for the steady regime of stage E.

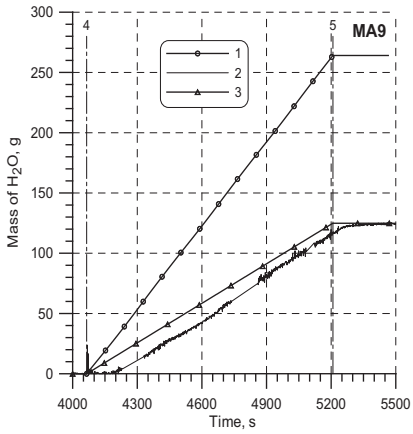

Fig. 5. Balance of steam and collected condensate in MA-9 test. (1) Steam into the furnace; (2, 3) collected condensate: (2) experiment, (3) interpolation taking transport delay into account; (4) start of steam supply into the furnace; (5) heating disconnection and stop of steam supply.

2.4. Experiment MCP-6

Like MCP-7, the MCP-6 experiment (Khabensky et al., 2011) was conducted within the METCOR-P project; but it is not fully analyzed in Sulatsky et al. (2013). Differently from MCP-7 the MCP-6 studied the oxidation of metallic, not oxidic, melt by steam. The melt has the following composition (mass%): SS – 64.5; U – 21.3; Zr – 14.2. The experiment was conducted using the technology of induction melting in a ceramic crucible. Zirconia concrete was chosen as the crucible material resistant to erosion and corrosion by a metallic melt. A schematic diagram of the furnace is given in Fig. 9.

To prevent steam penetration into the melt through crucible walls its outer surfaces were covered with alumosilicate enamel with ZrO_2 filling; its air-tightness was checked experimentally. The furnace was insulated from the ambient atmosphere by the quartz tube (Fig. 9, item 3).

To measure the temperature in the molten pool bulk two channels were drilled in the concrete crucible bottom; protective cases made of the same concrete were glued to them. W–Re thermocouples in tungsten sheaths were inserted into the protective cases. the temperature of concrete crucible walls and bottom was monitored by chromel–alumel thermocouples. The temperature of the crust on the metallic melt surface was measured by a pyrometer and a Pt–PtRh thermocouple in the alundum (fused alumina) sheath which was periodically inserted through the special port (Fig. 9, item 1).

Figs. 10–12 show readings of the temperature sensors, condensate weight strain gauge at the furnace exit and electrochemical hydrogen sensor after steam supply into the furnace and oxidation start. As can be seen, after the startup period, during which the surface crust was formed and inductor voltage was adjusted, indications of the temperature sensors and volumetric hydrogen concentration in the carrier gas at the furnace exit show the steady level (after 12,500 s).

Thermocouple TC05, which measures the temperature of metallic melt in the pool center along its axis, broke down at 11,000 s. But readings of TC06, the position of which was shifted to the periphery, did not give indications substantially different from those of TC05 at 11,000 s (Fig. 10), so TC06 readings can be used to evaluate the melt bulk temperature and its value during the steady-state regime (t > 13,000 s) is ~1400...1500 °C. Readings of TC07, which measured the surface crust temperature, is close to those of pyrometer T_{br1}, and during this regime the crust temperature was within ~1130...1250 °C (Fig. 10).

Readings of strain gauge given in Fig. 11 show a practically linear increase of condensate weight in the collector at the initial flow rate of steam supplied into the furnace (approximately 100 g H_2O/h (27.8 mg/s)) and considerable weight increase acceleration, when the flow rate of steam supply into the furnace was raised to approximately 200 g H_2O/h (55.6 mg/s).

In accordance with electrochemical hydrogen sensor (Fig. 12) during the steady state regime the steam flow rate increase does not lead to a noticeable change in the hydrogen release from the furnace. In these experimental conditions the metallic melt oxidation rate is quite insignificantly influenced by the flow rate of oxidant (steam) supplied to the furnace. The sharp increase of hydrogen content in the exit gases registered by the electrochemical sensor after the steam supply termination (Fig. 12) is explained by starting the supply of argon, which displaced the lighter hydrogen from the furnace.

During the post-experimental examination of crucible and ingot it was found that the surface ingot crust (Fig. 13) is not even, but covered with cracks, and metal droplets which were extruded from the melt during its oxidation and crystallized on solidification.

Fig. 14 shows the crucible axial section and ingot. Completed measurements of crucible walls showed the absence of their erosion (dissolution). Oxidic crust thickness on the ingot surface was 5 to 6 mm, side crust – 3–4 mm, and bottom crust – approximately 2 mm.

Crusts were separated from the ingot and weighed; the XRF and chemical analysis determined that they mostly consist of uranium and zirconium oxides. SEM/EDX analysis showed that the structure of surface crust has many pores and cracks, through which droplets of metal were extruded onto the crust surface. The crust phase composition showed the (U, Zr)O_2-based solid solution with very small amounts of α-Zr(O) and (U, Zr)Fe_2 (see Fig. 15).

Fig. 16 shows the measured and calculated rate of steam interaction with the melt, which was approximately 14 mg H_2O/s. Respectively, for the unit surface area the mass rate was 0.24 mg H_2O/(cm^2 s) (ingot surface area – 85 mm). Close values resulted from the calculation of oxygen mass necessary for the metal oxidation with oxidic crust formation. It should be noted that the increase of steam flow rate into the furnace did not change the rate of steam–melt interaction; this means that it is completely governed by the diffusion resistance of the surface oxidic crust.

2.5. Experiment MA-7

Experiment MA-7 (Asmolov et al., 2007) is different from MA-9 in the oxidant; air was supplied instead of steam at the 710 g/h

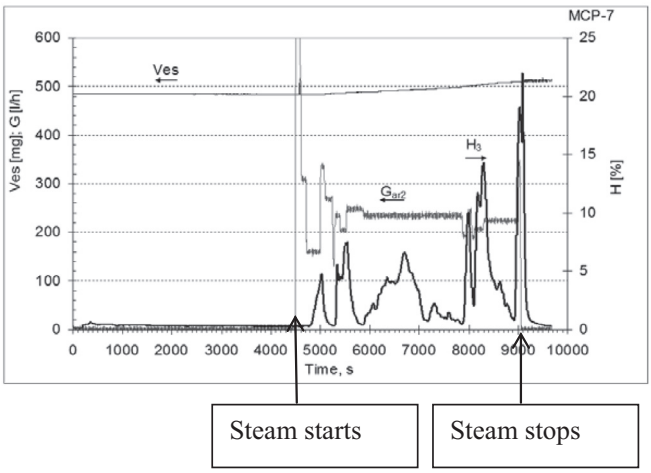

Fig. 6. Readings of condensate weight strain gauge (Ves), hydrogen sensor (H3) and carrier gas flow rate (Gar2) in MCP-7 test.

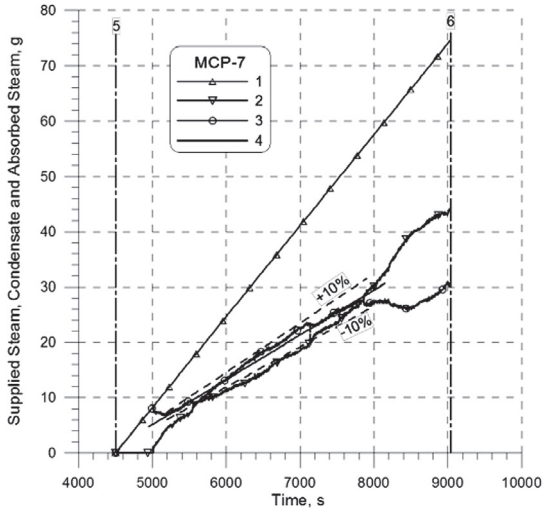

Fig. 7. Steam–melt interaction kinetics in MCP-7. (1) Steam in; (2) condensate out; (3) steam interacted with the melt; (4) approximation of steam–melt interaction in the steady regime; (5) steam supply start; (6) steam supply finish.

(197 mg/s) flow rate. The composition of the initial two-liquid pool is close to that of experiment MA-9 with a similar SS mass fraction – 0.1. Pool surface temperature was approximately 2500 °C. Exit gas composition was measured by the mass-spectrometer. Transport delay in the measured exit parameters was taken into account in the calculations of interaction rates for the air components and the melt (2), (3):

$$U/Zr + O_2 = UO_2/ZrO_2 \quad (2)$$

$$U/Zr + \frac{1}{2}N_2 = UN/ZrN \quad (3)$$

Figs. 17 and 18 show the calculated values of oxygen and nitrogen flow rates at the furnace entrance and exit. It can be seen that up to 3600 s oxygen is completely interacting with the melt; and the nitrogen almost completely with the melt: like oxygen it acts as an oxidant of melt components in accordance with (2), (3) The role of N_2 in its redox reaction with Zr is also discussed in Steinbrück et al. (2007) and Fischer and Levi (2010). In Fischer and Levi (2010) the authors discuss, in particular, separate oxidation of Zr-containing molten steel by air and steam. Fig. 19

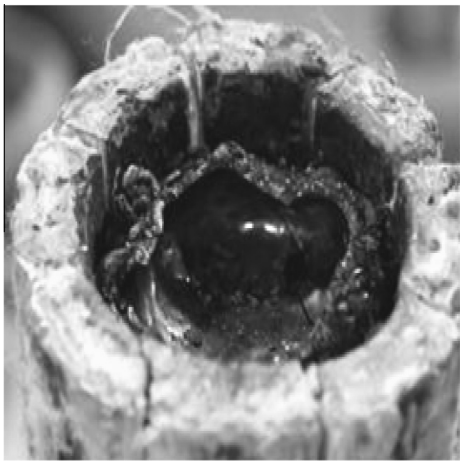

Fig. 8. Ingot top surface view during the furnace disassembly after MCP-7 test.

shows the change of air components, hence the melt interaction rate with the atmosphere. The decrease of interaction rate is explained by the crust formation on the pool surface observed on the surface central part at 3670 s, but Figs. 17–19 indicate that the formation started in the unobserved pool periphery already at 3600 s and that by 3700 s the crust covered the melt surface completely. It is also noted that there is a delay of approx. 200 s between the power supply cut-off and the response in the melt cooling and gas interaction rates. The interaction finally stops 300 s after the power cut-off.

In the course of surface crust formation the rate of O_2 and N_2 interaction with melt linearly decreases; then between 3600 s and 3750 s the melt oxidation goes through a slower stage. The rate of nitrogen–melt interaction decreases more rapidly and practically equals the oxygen–melt interaction rate. This change in reaction ratio is probably attributable to a better oxygen diffusivity through the crust, which, beside oxides, contains Zr and U nitrides. The interaction rate of air (components) with the melt calculated from experimental data in presence and absence of surface crust is:

- Firstly in crust absence ~1.17 mg O_2/(cm^2 s) and ~3.74 mg N_2/(cm^2 s), approximately in proportion to O_2 and N_2 content in air; so that the total mass rate of air–melt interaction is ~4.91 mg/(cm^2 s);
- Secondly in crust presence the mass rates of O_2 and N_2 interaction with melt are similar; they are ~0.52 mg/(cm^2 s), and the total mass rate of oxygen and nitrogen interaction, is then ~1.04 mg/(cm^2 s).

3. Discussion of results

Experimental conditions, results and data on the melt oxidation rates are summarized in Table 1 for comparison. For MCP-3 and MA-7 tests the characteristics of the two different experimental stages are given separately.

3.1. Melt oxidation kinetics

First, we should note that the results of «new» experiments MCP-6 and MCP-7 confirm conclusions of Sulatsky et al. (2013) that the oxidation rate does not depend on the concentration of the reducing agents (such as steel) in the melt, and these concentrations change with oxidation. This can be explained by the intensive convection in the inductively heated molten pool in cold crucible. The convection ensures the fast melt mixing accompanied by the even distribution of temperature and component concentrations

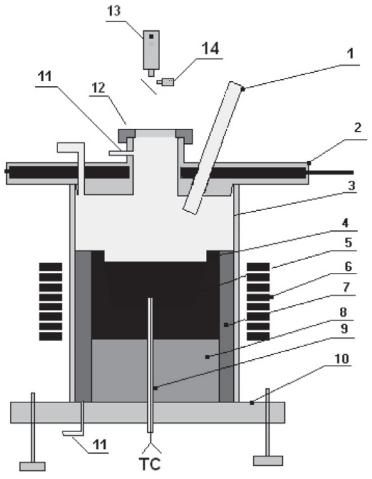

Fig. 9. MCP-6 furnace schematics. (1) two stainless steel ports for steam supply and for thermocouple measurements; (2) water-cooled furnace cover; (3) quartz tube; (4) zirconia concrete crucible; (5) metallic melt; (6) inductor; (7) ZrO_2 thermal insulation; (8) low-density thermal insulation of bottom; (9) W–Re thermocouple in the zirconia concrete sheath; (10) stainless steel base plate; (11) Ar supply port; (12) observation window cover; (13) pyrometer; (14) video camera.

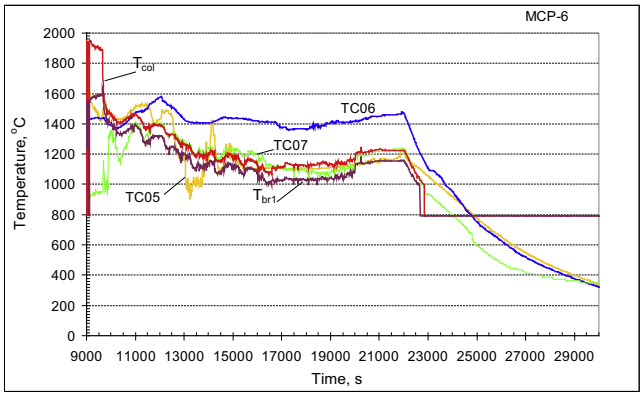

Fig. 10. Temperature readings in MCP-6 test. T_{col} and T_{br1}, color and brightness pyrometers; TC05 and TC06, W–Re thermocouples, which measured temperature in the bulk of metallic pool; TC07, Pt–Pt/Rh thermocouple, which measured the surface crust temperature.

in the pool. In the experimental conditions it leads to transport of reducing agent to the pool surface at a velocity which is much higher than the velocity of oxidant supply. The latter, in a general case, depends on the intensity of gas convection in the atmosphere above, chemical form of oxidant gases and their partial pressures. The most effective oxidant supply can be assumed for the case of water flooding.

Even without interfacial and top crusts, as in MA-9 with the two-liquid molten pool, the oxidation rate was sensitive neither to the mass of metallic liquid, which was decreasing in the course of oxidation (because of component partitioning between the metallic and oxidic melts), nor to the inversion of oxidic and metallic melts. It means that in conditions of intensive melt convection both the rate of oxidant transport from oxidic liquid to metallic liquid and the rate of components exchange between them are much higher than the rate of oxidant supply to the melt surface. The produced data lead to the conclusion that the equilibrium thermodynamic model can be used in case of molten pool oxidation transients, at least if there are no crusts between the molten layers.

An apparent exception is experiment MCP-3: though both experimental stages (C and E) had the same steam supply and molten pool surface conditions, at stage E (MCP-3(2)) in comparison with stage C (MCP-3(1)) the oxidation rate was two times lower. But it should be taken into account that stage E had the oxidation regime, when IZ was separated from the oxidic melt by the crust, which governed the oxidation rate reduction, being the diffusion barrier for the oxidant passing through the oxidic melt to the IZ. As at stage E the oxidation rate does not change to nearly complete oxidation of the IZ components; so we can conclude that this process (oxidant supply) also controls oxidation rate.

Let us first discuss results on the melt oxidation rate for the experiments, where steam was used as the oxidant. In this case oxygen comes into the redox reaction, and hydrogen is liberated as the gaseous product. The oxidation rate (per melt/oxidant interface unit area) can be derived either from the oxygen–melt reaction rate or from the hydrogen release rate or steam-melt interaction rate. Both of the latter differ from the oxygen-melt reaction rate by constant coefficients. The maximum level of steam–melt interaction was measured in MC-9 – 2.92 mg $H_2O/(cm^2\ s)$. In MCP-3(1) having the same conditions as MC-9, but approximately one-half the flow rate of supplied steam, MCP-3(1) had only an approximately 20% lower rate – 2.34 mg $H_2O/(cm^2\ s)$. These measurements were in situations of an upper crust-free surface, therefore the lower evaluated rate in MCP-3(1) in comparison with MC-9 can be explained, in this case, by the limited steam supply to the melt surface caused by the reduced steam flow in the furnace atmosphere.

A radical reduction of oxidation rate in comparison with MC-9 was observed in MCP-7 – 0.72 mg $H_2O/(cm^2\ s)$. Though this experiment had a different furnace dimensions and steam flow rate, the evident reason for such reduction is the presence of crust on the melt surface and the resulting critical limitation of oxidant access to the melt surface. In comparison with the access reduction related to the steam flow hydrodynamics in the above-melt atmosphere, the influence of surface crust diffusion resistance on the oxidant transport, even if the crust cracking is taken into account, proves to be the decisive factor in all realistic conditions where it occurs. The periodical cracking of crust with the melt extrusion, its spreading on the surface, oxidation and crystallization is confirmed by the video recording of crust surface. It is accompanied by a sharp increase in hydrogen release and surface temperature. Crack formation can be explained by the mechanical impact of the melt on the crust due to the melt expansion during oxidation. This depends on the ratio 'pool volume to the oxidant access surface area' and the crack generation intensity depends on the oxidation rate.

It should be noted that the crust on the oxidized IZ surface also existed in MCP-3(2), but the oxidation rate (1.17 mg $H_2O/(cm^2\ s)$) was much higher than in MCP-7. A possible reason for the difference can be in the specific conditions of MCP-3(2), under which the oxidant directly contacts the crust not in the gaseous, but in the liquid phase. The oxidation process in these conditions is, to a certain extent, similar to the corrosion of cooled vessel steel specimens in interaction with molten corium under oxidizing atmospheres, which was studied in Bechta et al. (2009).

An even stronger oxidation rate reduction in comparison with MCP-7 is observed in MCP-6 – 0.24 mg $H_2O/(cm^2\ s)$. In this experiment the metallic melt was subjected to oxidation, and, as the crust analysis revealed, mostly U and Zr contained in the melt were oxidized. Therefore, the melt surface was covered with the crust, consisting of their oxides. But in MCP-7 the average crust thickness was determined by the heat transfer phenomena and practically did not change, i.e. during oxidation the liquid oxides were formed and mixed with oxidic melt. In contrast to this in MCP-6 the crust thickness grew with time, because the melt temperature

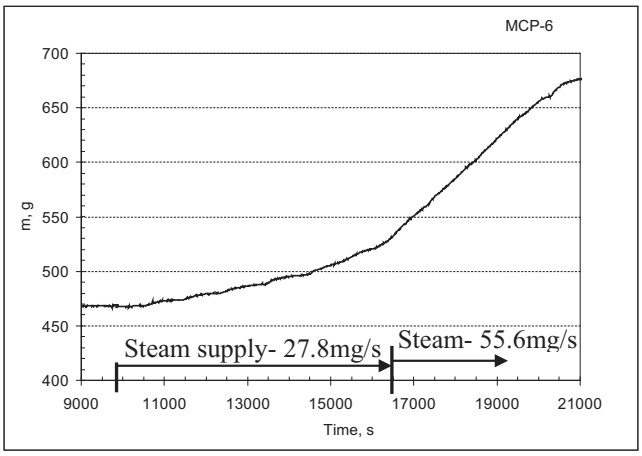

Fig. 11. Condensate weight measured by strain gauge in MCP-6 test.

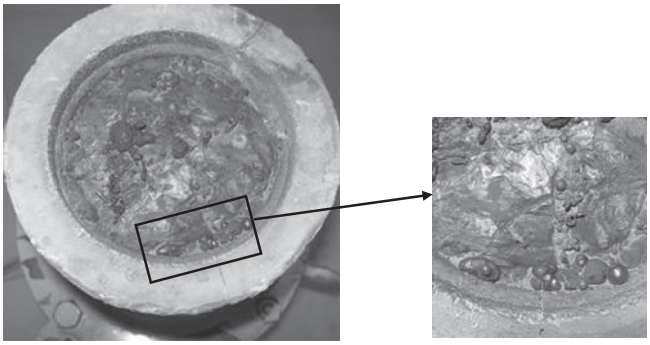

Fig. 13. Crust surface of MCP-6 solidified ingot.

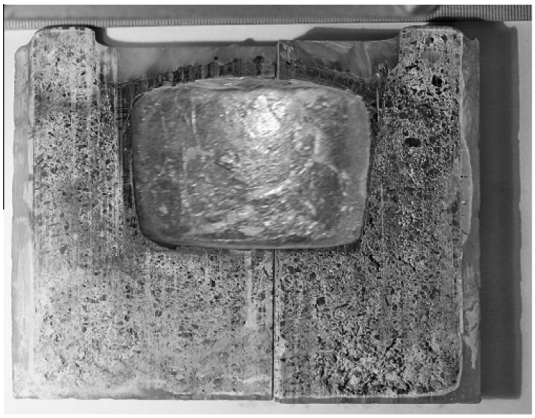

Fig. 14. Axial section of MCP-6 crucible with lateral view of metallic ingot.

(1400–1500 °C) was much lower than the UO_2–ZrO_2 system solidus. In spite of the crust thickness growth, the oxidation rate did not decrease versus time, which can be explained by the prevailing influence of crack formation on the mass transfer, like in MCP-7. Nevertheless, the difference of oxidation rates in the compared experiments is explained not by the different effective diffusion resistance of crusts, but by the difference in the phase condition of oxides formed. In contrast to MCP-7 liquid oxides the MCP-6 solid oxides can periodically clog the channels of oxidant supply to the melt and, on average compared to the melt surface and time, they can increase the upper crust's effective diffusion resistance and lead to a lower rate of oxidant supply to the melt.

On the other hand, comparing MCP-6 with MCP-3(2), in which the metallic melt was oxidized too, we can see that the MCP-6 oxidation rate is even lower in comparison with MCP-3(2) than MCP-7. The reason can be the same as discussed in the MCP-7 and MCP-3(2) comparison, i.e. the different state of the oxidant supplied to the crust. Possibly different crust cracking densities and solidification rates of the metallic melt in the cracks are factors. Once again we note that the MCP-3(2) conditions are quite specific and not characteristic for the melt oxidation in the reactor vessel.

Let us proceed to experiment MA-7, in which air was supplied into the furnace, not steam, so oxidants were oxygen and nitrogen (Sulatsky et al., 2013). Note that except the oxidant type, all conditions at the first stage of MA-7(1) in absence of crust on the melt surface were practically identical to those of MA-9. But the O_2 and N_2 – total melt interaction rates compared to that of steam–melt interaction rate (melt oxidation rate) are quite different. They are, respectively, 4.91 mg $(O_2 + N_2)/(cm^2\ s)$ and 2.76 mg $O_2/(cm^2\ s)$ (equal to 3.1 mg $H_2O/(cm^2\ s)$). The reason for lower oxidation rate by steam can be in the counter-current flow of hydrogen produced by the redox reaction, which hinders the oxygen access.

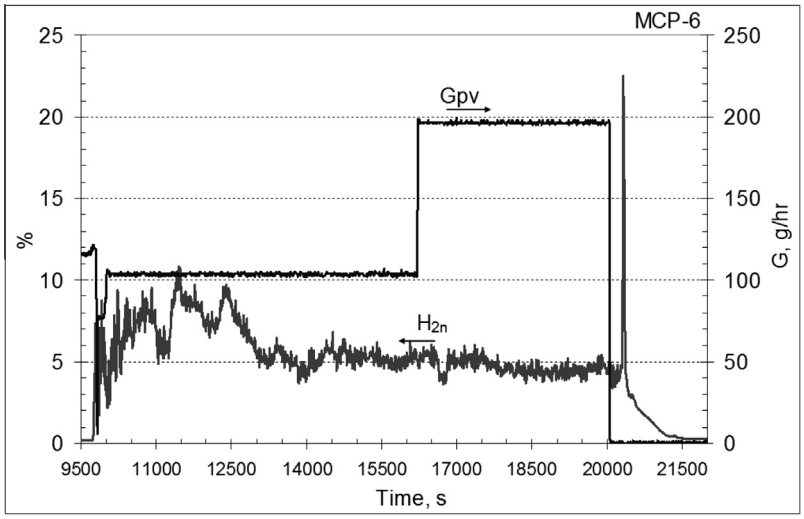

Fig. 12. Readings of electrochemical hydrogen sensor (H2n). and steam flow rate into the furnace (Gpv) in MCP-6 test.

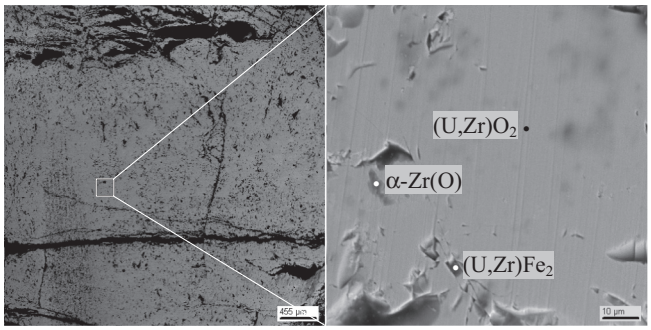

Fig. 15. MCP-6: the crust phase composition.

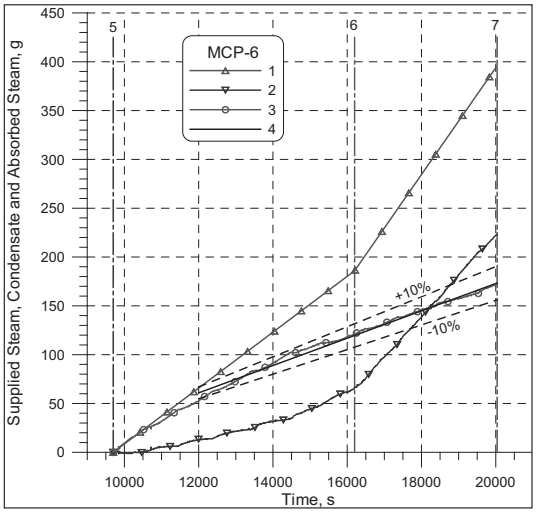

Fig. 16. Steam–melt interaction kinetics in MCP-6 test: (1) – supplied steam; (2) – condensate; (3) – steam interacted with melt; (4) – approximation of steam – melt interaction in the steady regime; (5) – steam supply start; (6) – increase of steam supply flow rate; (7) – termination of steam supply.

Considering oxidation regimes in presence of crust on the oxidic melt surface, we can compare the second stage of experiments MA-7(2) and MCP-7. Though all other conditions of these experiments have a substantial difference, the presence of crust, as mentioned above, is the decisive factor. We should mention in advance that in MA-7(1) the O/N-melt interaction rates were 1.17 mg O_2/(cm^2 s) and 3.74 mg N_2/(cm^2 s), and their ratio corresponds to their content in air (Sulatsky et al., 2013). In MA-7(2), as expected, both rates were lower, and the value was the same – 0.52 mg/(cm^2 s), i.e. the nitrogen – melt interaction rate decreased much more than that for oxygen. This can be explained by a worse N_2 transport through the crust, which, along with oxides, contains Zr and U nitrides. In this way, the MA-7(2) and MCP-7 interaction rates were, respectively, 1.04 mg (O_2 + N_2)/(cm^2 s) and 0.64 mg O_2/(cm^2 s) (equal to 0.72 mg H_2O/(cm^2 s)). It can be seen that the ratio of these rates is close to the same ratio for the crust-free oxidation regimes of MA-7(1) and MA-9, and the lower rate of oxidation by steam can also be explained by the blockage effect from hydrogen release.

3.2. Influence of melt oxidation on the in-vessel phenomena

Before applying the presented results to the IVR conditions, we should check if the thermodynamical equilibrium approximation could be used for modeling the molten pool structure and

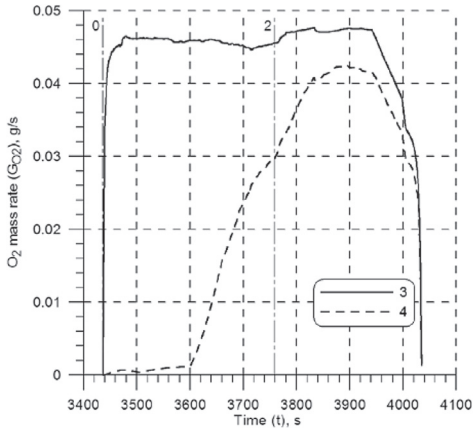

Fig. 17. Entrance and exit oxygen mass flow rates in the MA-7 test: (0) – air supply start; (2) – air supply termination and heating disconnection; (3) – entrance flow rate; (4) – exit flow rate.

composition during oxidation. For the discussed experimental conditions this conclusion mostly follows from the intensive melt convection.

During the induction heating power is deposited in rather thin layers of molten pool, mostly near the internal surface of the cold crucible. This results from the consecutive conversion of the electromagnetic energy into chaotic micro-eddy melt motion and further into the heat power in the mentioned pool layers. Therefore, like in the IVR, the melt motion is caused by the inhomogeneity of temperature and, consequently, of densities, i.e. it is the free convection dynamics. The influence of inhomogeneous induction heat deposition on the melt temperature inhomogeneity and, consequently, on the free convection intensity is an additional factor. It cannot be compared to the impact of the main factor expressed by the Ra number, which characterizes the free convection intensity. In the Rasplav-3 conditions the Ra number was 10^{10}...10^{13}, and for IVR conditions – 10^{15}...10^{16}, i.e. for the IVR conditions the intensity of melt free convection is even higher than for the completed experiments. Therefore, for the IVR conditions it is logical to make a conclusion that the oxidant supply rate to the crust-free surface is limiting with correspondingly steady melt oxidation rate and that the thermodynamical equilibrium approximation is suitable in the molten pool for modeling its oxidation.

Melt oxidation in the IVR conditions manifests itself as redox reactions accompanied by heat release and hydrogen generation. Hydrogen release rate in experiments can be directly evaluated from the steam–melt interaction rate presented in Table 1 multiplied by 1/9. For example for the MA-9 crust-free conditions on the oxidic-metallic pool surface the steam-melt interaction rate was the highest (2.92 mg H_2O/(cm^2 s)), and the maximum hydrogen release rate of 0.32 mg H_2/(cm^2 s) corresponded to this. In the experiments with the oxidic melt oxidation the minimum steam-melt interaction rate (0.72 mg H_2O/(cm^2 s)) was evaluated in MCP-7 in presence of surface crust, and the corresponding hydrogen release rate was 0.065 mg H_2/(cm^2 s).

In the evaluation of hydrogen release in the IVR conditions first it is necessary to note that the surface of two-liquid pool produced in the vessel bottom is invariably covered with crust, which almost completely consists of U and Zr oxides. This is explained by the high temperature of the system monotectics, which are 2300 to 2400 °C. Even in a hypothetical case of full oxidation of all metallic components of the melt (including SS components) its liquidus temperature will decrease to approximately 1900 °C, and the crust on the pool surface will stay though its composition will definitely change. Only at the initial stage of molten pool formation within

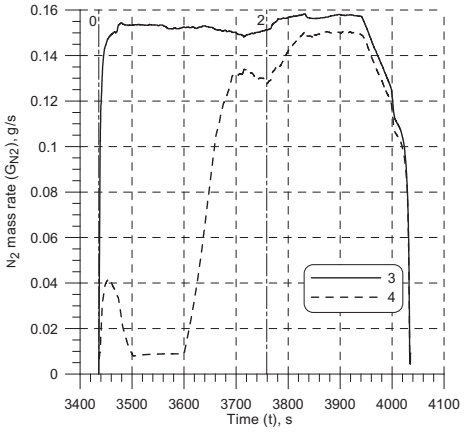

Fig. 18. Entrance and exit nitrogen mass flow rates in the MA-7 test. (0) – air supply start; (2) – air supply termination and heating disconnection; (3) – entrance flow rate; (4) – exit flow rate.

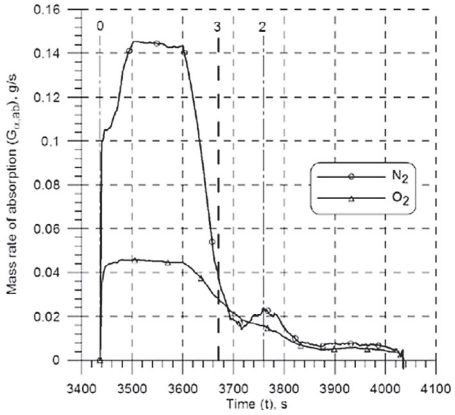

Fig. 19. Flow rates of air components interacting with melt in the MA-7 test. (0) – air supply start; (2) – air supply termination and heating disconnection; (3) – visually determined crust appearance (central pool).

the molten core, when the radiation from the surface is almost completely reflected, the crust is not formed.

Taking into account the above-mentioned factors, we believe that the most relevant situation for the evaluation of hydrogen release in the IVR conditions is when the steam is in contact with molten pool surface covered with crust. If we directly apply the MCP-7 data on the oxidation of two-liquid pool with the oxidic melt on top of a 4 m inner diameter of a reactor vessel, the hydrogen release rate would be approximately 30 kg/h. This is a fairly rough estimate because gas behavior above the melt in the experiment can differ from that in real reactor conditions. After oxide-metal layer inversion, an oxide crust forms at the molten metal surface. Hence, as the temperature of the surface metallic layer goes down, the oxidation rate drops considerably, as follows from the MCP-6 data. Using this, we can evaluate the hydrogen release minimum, which is approx. 10 kg/h.

Nevertheless, it should be taken into account that the crust cracking, which essentially influences its diffusion resistance, can be different in the real IVR conditions. The difference is explained by the scale factor, which changes both the impact of dynamic stresses from the oxidized melt on the crust and the strength of the crust itself. For this reason the experimental hydrogen release rate has a high degree of uncertainty when directly applied to the IVR conditions.

The MCP-7 data can also be used to evaluate the heat released at melt oxidation. As this experiment was terminated long time

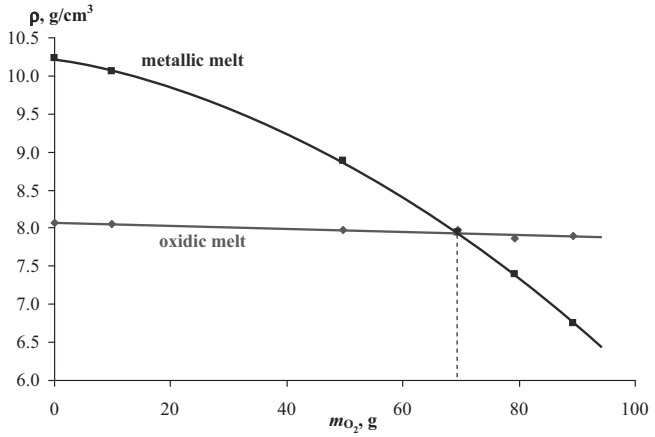

Fig. 20. Densities of oxidic and metallic melts vs. the mass of oxygen interacting with melt for MA-9 conditions.

before the full oxidation of the suboxidized corium melt, we can assume that the only relevant redox reaction was the Zr–steam interaction $Zr + 2H_2O = ZrO_2 + 2H_2$ accompanied by the heat release of reaction $\Delta H \approx 590$ kJ (at 2400 °C). In the recalculation for 1 g of H_2O the heat release is 16.4 kJ/g H_2O. Knowing that the flow rate of steam interacting with corium is 8.1 mg H_2O/s, we can evaluate heat deposition in the melt during oxidation, which is approximately 0.13 kW. If we take the melt density as about 8 g/cm^3, for the 1 kg ingot mass we get the 125 cm^3 melt volume. Then the volumetric density of heat deposition in the melt due to its oxidation is approximately 1 MW/m^3, which is commensurable with the decay heat density in the IVR conditions. We should note that in the IVR analysis the density of heat deposition resulting from oxidation is assumed to be much lower than the decay heat (though it requires evaluation), because in reactor conditions the ratio of oxidation surface area to the melt volume is much smaller in comparison with MCP-7.

Experimental data on the oxidation of two-liquid molten pool with the bottom position of metallic layer can be used to verify numerical evaluations of the oxidic and metallic layers inversion. For that we can use the MA-9 data. Though the exact time of the secondary inversion was not measured in this experiment, it could be determined indirectly using the measured evolution of integral heat flux into the bottom calorimeter placed below the molten pool.

In time step calculations the moment of inversion can be correlated with the time when densities of oxidic and metallic melts become equal assuming that component partitioning between them leads to a state of the two-liquid system close to thermodynamic equilibrium. Then we can calculate the average compositions of both molten pool layers versus corium oxidation which increases in time.

Calculations of the oxidic and metallic melt compositions were made using the GEMINI2 (Cheynet et al., 2002) code and thermodynamical database NUCLEA-06 (Cheynet and Fischer, 2006). Melt temperature corresponded to the experimental value, which was approximately 2500 °C. The molten layer densities can be estimated using an ideal law of mixing, which were derived from correlations (Eppinger et al., 2001). An exception was Zr oxide, for which the solid state density was taken from Journeau (2003) and diminished by 10%.

Fig. 20 shows the correlation of oxidic and metallic melt densities vs. the mass of adsorbed oxygen for the MA-9 conditions. The densities become equal at the absorbed oxygen mass of approximately 70 g. Fig. 21 shows the experimentally determined mass

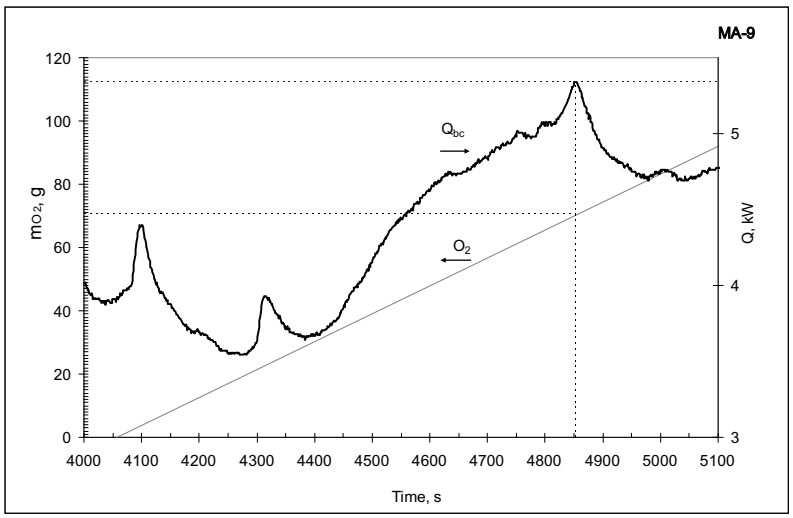

Fig. 21. Mass of interacting oxygen (O_2) and heat flux into the bottom calorimeter (Q_{bc}) vs. time for the MA-9 experiment.

of interacting oxygen and heat flux into the bottom calorimeter vs. time. It can be seen that 70 g of oxygen is absorbed approximately in 800 s after the melt oxidation, which agrees with the evaluated inversion moment, when the maximum heat flux value into the bottom calorimeter is reached. It should be mentioned that along with the gravitation forces, the melt is influenced by Lorenz forces generated by the induction field. They may introduce a certain error into the inversion moment calculations.

4. Conclusions

An experimental investigation into the kinetics of oxidation of a liquid by a gas is a complex problem because one has to simulate the thermo-fluid dynamic phenomena and mass transfer processes in reducing liquid and oxidizing gas phases and also the kinetics of reduction–oxidation reactions themselves. In the case of molten corium, however, the problem can be slightly simplified. Results of our new experiments confirm the previous conclusion (Sulatsky et al., 2013) that: (i) the rate of molten corium oxidation is controlled by the rate of oxidant supply into the reaction region and (ii) a thermodynamic equilibrium approximation can be applied in modeling.

If we leave aside melting of upper in-vessel structures under radiant heat flux and gradual metal melt relocation from the top i.e. 3-liquid pool formation possibility, the surface of the molten pool in the reactor vessel lower head is typically covered by an oxide crust. The experimental results have shown it is the crust diffusion resistance that reduces the oxidation rate and, thus, determines the oxidation kinetics. If the diffusion resistance of the surface crust represents the main limiting factor of oxidation kinetics, the processes occurring in the oxidizing phase do not require consideration.

On the other hand, for possible temporal cases with completely open melt surface, the oxidation kinetics will be controlled by the gas phase phenomena and transport phenomena in molten pool do not require much attention.

It is concluded that we can obtain oxidation kinetics data in experiments that represent real reactor conditions by developing a model crust at the melt surface. A model crust is a crust that has composition, thickness and temperature profile similar to those of a postulated crust forming under reactor conditions. While the crust with the required composition was obtained in our tests by using a prototypic corium, the required (real) crust thickness could not be finally achieved because of a possible difference in thermal conditions between experiment and the real reactor. However, the crust diffusion resistance is found to depend on integrity (cracking) rather than on thickness and the cracking may technically depend on the diameter of the molten pool. Nevertheless this oxidation kinetics data from a small-scale facility remains useful for obtaining estimates for numerical simulations of severe accident processes. Such estimates include the release of hydrogen, generation of heat in the melt pool, and layer inversion in the two-fluid stratified corium pool.

Larger scale experiments are needed to refine the available data and, if required, obtain more reliable new data.

However, the available experimental data is scarce and it is still important to continue experimental studies of molten corium oxidation using small-scale facilities. This is needed for understanding of the process mechanism and obtaining better estimates of the process kinetics, for example, the kinetics of oxidation during admission of water onto the crust at the melt surface under film boiling conditions and oxidation of the two-fluid corium with the metal layer on top.

Acknowledgements

This work has been partially funded by the EU through ISTC within the contract No. 3592.

References

Asmolov, V.G. et al., 2006. Main Results of the MASCA1 and 2 Projects//OECD//RRC. Kurchatov Institute.
Asmolov, V.G. et al., 2007. Molten corium stratification and component partitioning. In: Proc. of the MASCA2 Seminar, Sept. 11–12, 2007, Cadarache, France.
Bechta, S.V., Khabensky, V.B., Krushinov, E.V., et al., 2004. New experimental results on the interaction of molten corium with reactor vessel steel. In: Proc. of ICAPP'04, Pittsburgh, PA USA.
Bechta, S.V., Khabensky, V.B., Krushinov, E.V., et al., 2006. Experimental study of interaction between suboxidized corium and reactor vessel steel. In: Proc. of ICAPP06, Reno, USA.
Bechta, S.V., Granovsky, V.S., Khabensky, V.B., et al., 2009. VVER vessel steel corrosion at interaction with molten corium in oxidizing atmosphere. Nucl. Eng. Des. 239, 1103–1112.
Bechta, S.V. et al., 2010. Influence of corium oxidation on fission product release from molten pool. Nucl. Eng. Des. 240 (5), 1229–1241.
Cheynet, B., Fischer, E., 2006. Thermodata, Saint-Martin d'Hères.
Cheynet, B., Chevalier, P.Y., Fischer, E., 2002. Calphad 26, 167–174.
Eppinger, B., Fieg, G., Schmidt-Stiefel, S., Tromm, W., 2001. Investigations of the metallic and oxidic in-vessel corium densities: GEMINI2 calculations. IKET/FZK Report.

Fischer, M., Levi, P., 2010. The severe accident control strategy of the KERENA BWR. In: Proc. of ICAPP'10, San Diego, CA USA, June 13–17, Paper 10165.
Journeau, C., 2003. Physical properties density data for liquid corium. In: Presentation at the ECOSTAR Meeting, Berlin, Germany.
Khabensky, V.B. et al., 2003. Study of C-30 molten corium oxidation by atmospheric oxygen. ISTC Project-833.2 METCOR. Progress Report. Alexandrov Research Institute of Technologies (NITI), Sosnovy Bor, Russia.
Khabensky, V.B. et al., 2011. Investigation of corium melt interaction with NPP reactor vessel Steel (METCOR-P). Project # 3592, ISTC. Intermediate report: Test MCP-3.
Khabensky, V.B. et al., 2011. Investigation of corium melt interaction with NPP reactor vessel steel (METCOR-P). Project # 3592, ISTC. Intermediate report: Tests MCP-6. MCP-7.
Steinbrück, M., Stegmaier, U., Ziegler, T., 2007. Prototypical Experiments on Air Oxidation of Zircaloy-4 at High Temperatures, Wissenschaftliche Berichte FZKA 7257. Forschungszentrum Karlsruhe GmbH, Karlsruhe.
Sulatsky, A.A., Smirnov, S.A., Granovsky, V.S., et al., 2013. Oxidation kinetics of corium pool. Nucl. Eng. Des. 262, 168–179.